
ALMA and RATIR observations of GRB131030A

Kuiyun Huang¹, Yuji Urata², Satoko Takahashi^{3,4}, Myungshin Im⁵,
Po-Chieh Yu¹, Changsu Choi⁵, Nathaniel Butler⁶, Alan M. Watson⁷,
Alexander Kutyrev⁸, William H. Lee⁷, Chris Klein⁹, Ori D. Fox^{9,10}, Owen
Littlejohns⁶, Nino Cucchiara⁸, Eleonora Troja^{11,8}, Jesús González⁷,
Michael G. Richer⁷, Carlos Román-Zúñiga⁷, Josh Bloom⁹, J.Xavier
Prochaska¹², Neil Gehrels⁸, Harvey Moseley⁸, Leonid Georgiev⁷, José A.
de Diego⁷, Enrico RamirezRuiz¹²

¹Department of Mathematics and Science, National Taiwan Normal University, Lin-kou
District, New Taipei City 24449, Taiwan

²Institute of Astronomy, National Central University, Chung-Li 32054, Taiwan

³Joint ALMA Observatory, Alonso de Cordova 3108, Vitacura, Santiago, Chile

⁴National Astronomical Observatory of Japan, 2-21-1 Osawa, Mitaka, Tokyo 181-8588, Japan

⁵Center for the Exploration of the Origin of the Universe, Department of Physics & Astronomy,
FPRD, Seoul National University, Shillim-dong, San 56-1, Kwanak-gu, Seoul, Korea

⁶School of Earth & Space Exploration, Arizona State University, Tempe, AZ 8528

⁷Instituto de Astronomía, Universidad Nacional Autónoma de México, Apartado Postal
70-264, 04510 México, D. F., México

⁸NASA, Goddard Space Flight Center, Greenbelt, MD 20771

⁹Astronomy Department, University of California, Berkeley, CA 94720-7450

¹⁰Space Telescope Science Institute, 3700 San Martin Drive, Baltimore, MD 21218

¹¹Department of Astronomy, University of Maryland, College Park, MD 20742

¹²Department of Astronomy and Astrophysics, UCO/Lick Observatory, University of

Abstract

We report on the first open-use based Atacama Large Millimeter/submm Array (ALMA) 345-GHz observation for the late afterglow phase of GRB131030A. The ALMA observation constrained a deep limit at 17.1 d for the afterglow and host galaxy. We also identified a faint submillimeter source (ALMAJ2300-0522) near the GRB131030A position. The deep limit at 345 GHz and multifrequency observations obtained using *Swift* and RATIR yielded forward shock modeling with a two-dimensional relativistic hydrodynamic jet simulation and described X-ray excess in the afterglow. The excess was inconsistent with the synchrotron self-inverse Compton radiation from the forward shock. The host galaxy of GRB131030A and optical counterpart of ALMAJ2300-0522 were also identified in the SUBARU image. Based on the deep ALMA limit for the host galaxy, the $3\text{-}\sigma$ upper limits of IR luminosity and the star formation rate (SFR) is estimated as $L_{IR} < 1.11 \times 10^{11} L_{\odot}$ and $\text{SFR} < 18.7 (M_{\odot} \text{ yr}^{-1})$, respectively. Although the separation angle from the burst location ($3''.5$) was rather large, ALMAJ2300-0522 may be one component of the GRB131030A host galaxy, according to previous host galaxy cases.

Key words: gamma-ray burst: individual (GRB131030A) — Submillimeter: galaxies — X-rays: bursts

1 Introduction

Submillimeter (submm) and millimeter (mm) follow-up observations have played an essential role in identifying gamma-ray burst (GRB) afterglow and host galaxies in, for example delineating the energy scale, geometry, radiation physics, and environments of long GRBs (e.g. Frail et al. 2002; Sheth et al. 2003; Urata et al. 2014). However, submm/mm follow-up observations have lagged behind X-ray, optical and cm radio observations (summaries of afterglow observations are available in de Ugarte Postigo et al. 2012; Urata et al. 2015a) because of the limited sensitivity of previous submm/mm facilities coupled with the higher redshift of *Swift* GRBs.

The Atacama Large Millimeter/submm Array (ALMA) was first used in the early science phase for GRB host galaxies, and its observations have provided exceptional results (Wang et al.

2012; Hatsukade et al. 2014; Berger et al. 2014). However, observations for afterglow phase are still limited because of the observation guidelines of ALMA (e.g. a 3-week reaction time since ToO triggering) for the early science phase (e.g. Cycle 1). Here, we report the first open-use based ALMA observation of the late afterglow phase of GRB131030A.

GRB 131030A was detected using the *Swift* (Gehrels et al. 2004) Burst Alert Telescope (BAT) at 20:56:18 UT on 2013 October 30 (Troja et al. 2013). The duration, T_{90} in the 15–350 keV band was 41.1 ± 4.0 s (Barthelmy et al. 2013). The afterglow in X-ray and optical bands was also identified using the *Swift* X-ray Telescope (XRT) and Ultraviolet/Optical Telescope (UVOT). On the basis of the UVOT observation, the burst position was determined at $23^{\text{h}}00^{\text{m}}16^{\text{s}}.14$, $-05^{\circ}22'05''.2$ with a 90% confidence error radius of $0''.5$ (Breeveld & Troja 2013). The redshift of GRB 131030A was measured at $z = 1.293$ on the basis of the optical spectroscopic observation by using the Nordic Optical Telescope (Xu et al. 2013). The polarized early (655s to 2 hrs) optical lightcurve of the afterglow was also observed using the RoboPol instrument (King et al. 2014). The Konus-Wind observation also revealed a prompt emission and characterized the spectrum properties in the 20 keV – 15 MeV range. The time-averaged spectrum was fitted using the Band function with the spectrum peak energy $E_{\text{peak}}^{\text{obs}}$ of 177 ± 10 keV. The isotropic energy E_{iso} was also estimated as $(3.0 \pm 0.2) \times 10^{53}$ erg, assuming cosmological parameters of $H_0 = 70 \text{ km s}^{-1} \text{ Mpc}^{-1}$, $\Omega_m = 0.27$, and $\Omega_\Lambda = 0.73$ (Golenetskii et al. 2013).

2 Observations and Results

2.1 ALMA Submillimeter Follow-up Observation

We used ALMA to observe the afterglow at 345-GHz (default continuum setup) with the C32-5 configuration under the Cycle 1 open-use mode. Although the observation policy of the ALMA Cycle 1 includes a 3-week reaction time restriction for its execution through ToO triggering, the 345-GHz observation was initiated at 23:11 UT on 2013 November 16 (17.12 d after the GRB). Thus, the observation was executed several days earlier than expected. Three calibrators (J2232+117, J2148+0657, and J2301–0158) for flux, bandpass, and phase calibrations, respectively, were also observed. The on-source time and total observing time were 53 min and 90 min, respectively. The raw data were calibrated using the Common Astronomy Software Applications 4.1 (CASA, McMullin et al. 2007) with the standard procedure, and final CLEANed images were made using the “clean” task with a robust briggs weighting (robust parameter of 0.5). The resulting synthesized beam sizes were $0''.252 \times 0''.207$ with a position angle of 68.2 deg. No source was observed from the location of the optical afterglow to the $3\text{--}\sigma$ limit of 0.12 mJy (Figure 1 left). As shown in Figure 2, this limit is significantly deep in

the submm bands among other afterglow observations. Although ALMA observed the bright submm afterglow associated with GRB110715A (~ 5 mJy at 3.6 d) during the commissioning phase (de Ugarte Postigo et al. 2012), the quality of observation was comparable with those of other smaller submm instruments. Hence, this demonstration of the high sensitivity follow-up would be a benchmark with further submm observations. As shown in Figure 1 (left), a source (ALMAJ2300-0522) with 0.716 ± 0.045 mJy was identified in the ALMA image at $23^{\text{h}}00^{\text{m}}16^{\text{s}}.326$, $-05^{\circ}22'07''.50$ (approximately $3''.5$ from the GRB position). Although several astrometry-related bugs (e.g. phase calibrator coordinate inconsistency) were reported from the ALMA ARC after data delivery, we could not reasonably explain the significant offsets of approximately $3''.5$ (more than 10-fold the beam size) from the GRB position. In addition, the source also had an optical counterpart in the SUBARU *Rc*-band image (Figure 1 right, §2.5).

2.2 Optical and Near Infrared Afterglow Follow-ups

We used the Reionization and Transients InfraRed camera (RATIR) to monitor the afterglow in *r*-, *i*-, *Z*-, *Y*-, *J*- and *H*-bands from 1.763×10^4 s to 7.220×10^5 s after the burst. RATIR is a six band simultaneous optical and NIR imager mounted on the autonomous 1.5 m Harold L. Johnson Telescope at the Observatorio Astronómico Nacional on Sierra San Pedro Mártir in Baja California, Mexico (Butler et al. 2012; Watson et al. 2012; Klein et al. 2012; Fox et al. 2012). The images were reduced in near real-time using an automatic pipeline. Bias subtraction and twilight flat division were performed using algorithms written in PYTHON, image alignment was conducted by astrometry.net (Lang et al. 2010) and image co-addition was achieved using SWARP (Bertin 2010).

We performed photometry for individual science frames and mosaic using SEXTRACTOR (Bertin & Arnouts 1996) with apertures ranging from 2 to 30 pixels ($0''.64 - 9''.6$ in optical, $0''.6 - 9''.0$ in NIR). Based on the weighted average of the flux in these apertures for all stars in a field, an annular point-spread-function (PSF) was constructed. We then optimized point source photometry by fitting this PSF to the annular flux values of each source. The photometric calibration in *r*-, *i*-, *Z*-, *J* and *H* bands were made comparing with the Sloan Digital Sky Survey Data Release 9 (SDSS) and the Two Micron All Sky Survey. The RATIR and SDSS *r*-, *i*- and *Z*-bands agree to within $\lesssim 3$ per cent (Butler et al. 2016 in prep.). For the *Y*-band calibration, we used an empirical relation in terms of *J* and *H* magnitudes derived from the United Kingdom Infrared Telescope (UKIRT) Wide Field Camera observations (Hodgkin et al. 2009; Casali et al. 2007).

We also conducted the *B*- and *R*-band follow-up observations by using the robotic 1-m telescope at the Mt. Lemmon observatory, which is operated by the Korea Astronomy Space Science

Institute (Lee et al. 2010; Han et al. 2005). The observations were initiated at 01:43 UT on 2013 October 31 (1.720×10^4 s after the burst), and three epochs for monitoring were conducted during the same run. A standard routine including bias subtraction and flat-fielding corrections was employed to process the data using the IRAF package. The DAOPHOT package was used to perform aperture photometry of the GRB images. For the photometric calibration of the afterglow, several stars from the NOMAD catalog¹ were chosen. To remove the effects of the Galactic interstellar extinction, we used the reddening map by Schlafly & Finkbeiner (2011).

2.3 Afterglow Lightcurve

The multifrequency lightcurve is shown in Figure 3 (left). The X-ray data were obtained from the online data repository prepared by Butler & Kocevski (2007). The temporal evolution in the r - and i -bands indicates an achromatic temporal break at approximately $\sim 2 \times 10^5$ s. In contrast, X-ray light curve later than $\sim 4 \times 10^3$ sec shows the simple evolution. To describe the light curves, we employed a single power-law function by dividing light curve data into earlier ($t < \sim 2 \times 10^5$) and later ($t > \sim 2 \times 10^5$) phases. We successfully fitted the single power-law function to the earlier light curves. The r -, i -, and X-ray band light curves in the later phase were also described using the single power law function. The X-ray light curve later than $\sim 4 \times 10^3$ sec was also described with the single power-law function with the decay index of $\alpha_X = -1.25 \pm 0.02$. Here, we use a notation $F_\nu \propto t^\alpha \nu^\beta$ with sub-indices of observed band. The fitting results are summarized in Table 1. We also successfully fitted the broken power-law model to the r - and i -bands light curves. For the r -band, we obtained $\alpha_{r1} = -0.86 \pm 0.04$, $\alpha_{r2} = -2.06 \pm 0.16$, and $t_{br} = (2.51 \pm 0.48) \times 10^5$ s; for the i -band, we obtained $\alpha_{i1} = -0.82 \pm 0.04$, $\alpha_{i2} = -2.04 \pm 0.17$, and $t_{bi} = (2.51 \pm 0.48) \times 10^5$ s. Here, sub-indices of 1 and 2, and t_b indicate before and after the temporal break, and the break time, respectively. The decay index of X-ray afterglow before the jet break is also estimated as $\alpha_{X1} = -1.31 \pm 0.04$.

2.4 Afterglow Spectrum

We generated spectral flux distributions at 2.32×10^4 s (0.268 d; first epoch) and 3.76×10^5 s (4.34 d; second epoch). For the first epoch, we also added $UVW2$ -, U -, B -, and V -band data that were obtained using *Swift*/UVOT at approximately 2.3×10^4 s after the burst, which coincided with the RATIR observations. We used the standard procedure for the UVOT analysis². As shown in Figure 3 (right), the sharp spectral drop at approximately 1×10^{15} Hz that was caused by the $\text{Ly}\alpha$ absorption at $z = 1.293$ was identified. Thus, we fitted the first epoch SED with a power-law function by excluding

¹ <http://www.usno.navy.mil/USNO/astrometry/optical-IR-prod/nomad>

the *UVW2* data and obtained $\beta = -0.57 \pm 0.09$ ($\chi^2/\nu = 1.9$ with $\nu = 8$) for the first epoch and $\beta = -1.08 \pm 0.23$ ($\chi^2/\nu = 0.34$ with $\nu = 3$) for the second epoch. As shown in Figure 3 (right), the optical SED, including the UV data points obtained using UVOT, were effectively described by the single power-law function without considering the host galaxy extinction.

2.5 SUBARU Archive Image and Host Galaxy

We reduced the SUBARU Suprime-Cam images obtained from the SMOKA archive system (Baba et al. 2002). The GRB131030A field was observed using the *Rc*-bands during the previous follow-up observations of XRF040916 on September 20, 2004. Owing to the wide field of view of the Suprime-Cam (Miyazaki et al. 2002), the location of GRB 131030A had an effective exposure time of 2400 s. The basic reduction of the Suprime-Cam data was performed using the SDFRED (Ouchi et al. 2004). The final coadded image was astrometrically aligned relative to the SDSS catalog, resulting in an rms scatter of $0''.08$. Figure 1 (right) provides the *Rc*-band images for the GRB131030A field, and an extended source was identified inside the position error region through *Swift*/UVOT. By using IRAF centroid, the location of the source was determined at $23^{\text{h}}00^{\text{m}}16^{\text{s}}.146$, $-05^{\circ}22'05''.18$, which is $0''.07$ away from the afterglow location. The projected offset of 0.6 kpc is smaller than values for long GRBs (e.g. Bloom et al. 2002). Thus, we concluded that the source was the host galaxy of GRB131030A. The brightness with a $1''.0$ radius was $R_c = 26.23 \pm 0.11$. The optical counterpart of ALMAJ2300-0522 was also measured as $R_c = 24.48 \pm 0.03$ with a $1''.6$ radius.

3 Discussions

3.1 Forward Shock Radiation and X-Ray Excess

The multicolor monitoring observations performed using RATIR provided an effective dataset for describing the forward shock synchrotron radiation. The spectral index change between first and second epochs could be due to the cooling frequency passage in the optical band. The absence of the sharp cooling break in the optical light curves could be explained by the smooth transition of spectral regimes (e.g. Uhm & Zhang 2014). The closure relation (e.g. Sari et al. 1999) also indicated that the optical afterglow at 2.32×10^4 s and 1.56×10^5 s was consistent with $\nu_m < \nu_{\text{opt}} < \nu_c$ under the interstellar medium (ISM) with a slow cooling condition ($\alpha = 3/2\beta = -0.86 \pm 0.14$) and jet phase with $nu_{\text{opt}} > \nu_c$ ($\alpha = 2\beta = -2.2 \pm 0.5$), respectively. Although the optical afterglow showed the jet break, the X-ray afterglow revealed no temporal break at the jet break time. The $\alpha_o - \alpha_x$ relation of 0.44 ± 0.06 for before the jet break was also the explicit outlier (e.g. Urata et al. 2007). Thus, these

² <http://www.swift.ac.uk/analysis/uvot/index.php>

results indicate that the X-ray afterglow could have an origin that was distinct from that of the optical afterglow (e.g. Huang et al. 2007; Troja et al. 2007).

To describe the X-ray afterglow behavior, we performed forward shock synchrotron radiation modeling with the optical light curves and ALMA upper limit by using the boxfit code (van Eerten et al. 2012). Because the code involved a two-dimensional relativistic hydrodynamical jet simulation with a homogeneous circumburst medium, we hereafter, consider only the ISM condition. We determined the optimal modeling parameters with the on-axis case (observing angle, $\theta_{obs}=0$) as $\theta_{jet}=8^\circ.8$, $E = 1.05 \times 10^{52}$ erg, $n = 2.54 \times 10^{-1}$ cm $^{-3}$, $p=2.28$, $\epsilon_B = 4.36 \times 10^{-2}$, and $\epsilon_e = 2.69 \times 10^{-1}$. The values were updated from those in Urata et al. (2015b) by using data from six OIR bands and the ALMA 1- σ limit. Figure 3 shows the most effective model functions for multicolor light curves. The broadband SED modeling results are also provided in Figure 4. These results clearly show the excess in the X-ray band.

On the basis of the analytic solution described by Fan et al. (2008), we calculated the expected flux density of synchrotron self-inverse-Compton radiation (SSC) by using forward shock modeling. The reasonable flux scale and differences (approximately 10-fold times) between synchrotron and SSC for the earlier afterglow were estimated using the model. However, the SSC model could not explain the different temporal evolution in the late phase. In addition, the expected ν_m^{SSC} pass in the X-ray band ($\sim 4 \times 10^5$ sec) with the analytic solution was not identified in the observed X-ray spectrum (Figure 5). Hence, SSC is unlikely to explain the observational properties. One of the alternative models for describing the distinct temporal evolution between optical and X-ray is the late prompt emission (Ghisellini et al. 2007). A spinning-down magnetar as the central engine is one of the explanations for the X-ray excess (Zhang & Mészáros 2001; Troja et al. 2007).

3.2 Host Galaxy and ALMAJ2300-0522

The ALMA observation also provides a unique upper limit of 345-GHz for estimating the rest-frame infrared luminosity and star formation rate (SFR) of the host galaxy. Following Wang et al. (2012), we applied a redshifting to a template infrared SED, which we obtained from the library provided by Chary & Elbaz (2001). The SED library is luminosity-dependent (2×10^8 to $4 \times 10^{13} L_\odot$) based on a locally calibrated luminosity-dust temperature relation and does not enable scaling the SEDs. We constrained the 3- σ upper limits of IR luminosity as $L_{IR} < 1.11 \times 10^{11} L_\odot$. Using the SFR conversion of star-forming galaxies, $\text{SFR}(M_\odot \text{ yr}^{-1}) = 1.7 \times 10^{-10} L_{IR}/L_\odot$ (Kennicutt 1998) used in Wang et al. (2012), we obtained the 3- σ upper limit of SFR as $< 18.7 (M_\odot \text{ yr}^{-1})$. The upper limit of SFR was consistent with those of the TOUGH samples that constrained the average SFR as lower than 15

$M \odot \text{ yr}^{-1}$ (Hjorth et al. 2012; Michałowski et al. 2012).

ALMAJ2300-0522 is $3''.5$ (30.2 kpc) from the GRB location. Some of the GRB host galaxies show companions and exceptionally extended emission. HST images resolved companions for GRB021004 at $0''.28$ (2.4 kpc) from the host location (Fynbo et al. 2005), for GRB050820A at $1''.3$ (10.7 kpc) (Chen et al. 2009) and $0''.4$ (3.3 kpc), and for GRB080605 at $1''.0$ (8.7 kpc) (Krühler et al. 2012), respectively. Most notably, the $\text{Ly}\alpha$ imaging for the GRB000926 host galaxy revealed extended emission of approximately 33.7 kpc at the long axis (Fynbo et al. 2002). Thus, ALMAJ2300-0522 is potentially a component of the GRB131030A host galaxy. By assuming the same redshift with GRB131030A, we also obtained $L_{\text{IR}} = 8.65 \times 10^{11} L_{\odot}$ and the corresponding SFR of $147 M_{\odot} \text{ yr}^{-1}$ by using the same template redshifting method (green solid line in Figure 6). The obtained values were comparable or lower than those of observed ultra luminous infrared galaxy host cases (e.g. Berger et al. 2001; Frail et al. 2002).

Another noteworthy feature is that ALMAJ2300-0522 is categorized as a faint (<1 mJy) submm galaxy (SMG). Faint SMGs tend not to have optical counterparts, in contrast to ALMAJ2300-0522, even when ultra-deep optical survey data are used (Chen et al. 2014; Ono et al. 2014; Fujimoto et al. 2016). Hence, future studies that use redshift estimation can clarify the SMG-GRB association.

4 Conclusion and Summary

We conducted the first open-use based ALMA observation for the afterglow of GRB131030A. The high sensitivity of the ALMA observation would make a significant improvement in further afterglow follow-ups such as coordinated submm observations for radio polarimetry and longterm multi-frequency monitoring. With the comprehensive optical and near infrared afterglow observations performed through RATIR, we described the forward shock synchrotron radiation and X-ray excess in the afterglow. The excess is inconsistent with the SSC model and requires another component such as late prompt emission. Our ALMA observation also constrains the $3\text{-}\sigma$ limit of infrared luminosity and SFR of the host galaxy, which is consistent with other nearby $z < \sim 1$ samples. The submm source, ALMAJ2300-0522 is located $3''.5$ from the GRB location. Although the separation is rather large, the source may be one component of the host galaxy, according to previous host galaxy cases (e.g. GRB000926). To further analyze the association between ALMAJ2300-0522 and GRB131030A, secure redshift estimation is required.

Acknowledgments

This paper makes use of the following ALMA data: ADS/JAO.ALMA#2012.1.00875.T. ALMA is a partnership of ESO (representing its member states), NSF (USA) and NINS (Japan), together with NRC (Canada), NSC and ASIAA (Taiwan), and KASI (Republic of Korea), in cooperation with the Republic of Chile. The Joint ALMA Observatory is operated by ESO, AUI/NRAO and NAOJ. We also thank EA-ARC, especially Shigehisa Takakuwa and Trejo-Cruz Alfonso for various supports on ALMA observation and reduction. This work is partly supported by the Ministry of Science and Technology of Taiwan grants MOST 104-2112-M-008-011 and 105-2112-M-008-013-MY3 (YU). We thank the RATIR project team and the staff of the Observatorio Astronómico Nacional on Sierra San Pedro Mártir. RATIR is a collaboration between the University of California, the Universidad Nacional Autónoma de México, NASA Goddard Space Flight Center, and Arizona State University, benefiting from the loan of an H2RG detector and hardware and software support from Teledyne Scientific and Imaging. RATIR, the automation of the Harold L. Johnson Telescope of the Observatorio Astronómico Nacional on Sierra San Pedro Mártir, and the operation of both are funded through NASA grants NNX09AH71G, NNX09AT02G, NNX10AI27G, and NNX12AE66G, CONACyT grants INFR-2009-01-122785 and CB-2008-101958, UNAM PAPIIT grant IG100414 and CONACyT LN260369, and UC MEXUS-CONACyT grant CN 09-283. MI and CC acknowledge the support from the National Research Foundation of Korea grant, No. 2008-0060544, funded by the Korea government (MSIP). This work made use of data supplied by the UK Swift Science Data Centre at the University of Leicester.

References

- Baba, H., et al., 2002, ASP Conference Series, Vol. 281, 298
- Barthelmy, S. D., Baumgartner, W. H., Cummings, J. R., et al. 2013, GRB Coordinates Network, 15456, 1
- Berger, E., Kulkarni, S. R., & Frail, D. A. 2001, ApJ, 560, 652
- Berger, E., Zauderer, B. A., Chary, R.-R., et al. 2014, ApJ, 796, 96
- Bertin, E., & Arnouts, S. 1996, A&AS, 117, 393
- Bertin, E. 2010, Astrophysics Source Code Library, 1010.068
- Bloom, J. S., Kulkarni, S. R., & Djorgovski, S. G. 2002, AJ, 123, 1111
- Breeveld, A. A., & Troja, E. 2013, GRB Coordinates Network, 15414, 1
- Butler, N. R., & Kocevski, D. 2007, ApJ, 663, 407
- Butler, N., Klein, C., Fox, O., et al. 2012, Proc. SPIE, 8446, 844610
- Casali, M., Adamson, A., Alves de Oliveira, C., et al. 2007, A&A, 467, 777
- Chary, R., & Elbaz, D. 2001, ApJ, 556, 562
- Chen, H.-W., Perley, D. A., Pollack, L. K., et al. 2009, ApJ, 691, 152
- Chen, C.-C., Cowie, L. L., Barger, A. J., Wang, W.-H., & Williams, J. P. 2014, ApJ, 789, 12
- van Eerten, H., van der Horst, A., & MacFadyen, A. 2012, ApJ, 749, 44
- Fan, Y.-Z., Piran, T., Narayan, R., & Wei, D.-M. 2008, MNRAS, 384, 1483
- Fox, O. D., Kuttyrev, A. S., Rapchun, D. A., et al. 2012, Proc. SPIE, 8453, 84531O
- Frail, D. A., Bertoldi, F., Moriarty-Schieven, G. H., et al. 2002, ApJ, 565, 829

Fujimoto, S., Ouchi, M., Ono, Y., et al. 2016, *ApJS*, 222, 1

Fynbo, J. P. U., Möller, P., Thomsen, B., et al. 2002, *A&A*, 388, 425

Fynbo, J. P. U., Gorosabel, J., Smette, A., et al. 2005, *ApJ*, 633, 317

Gehrels, N., Chincarini, G., Giommi, P., et al. 2004, *ApJ*, 611, 1005

Ghisellini, G., Ghirlanda, G., Nava, L., & Firmani, C. 2007, *ApJL*, 658, L75

Golenetskii, S., Aptekar, R., Frederiks, D., et al. 2013, *GRB Coordinates Network*, 15413, 1

Han, W., et al. 2005, *PASJ*, 57, 821

Hatsukade, B., Ohta, K., Endo, A., et al. 2014, *Nature*, 510, 247

Hjorth, J., Malesani, D., Jakobsson, P., et al. 2012, *ApJ*, 756, 187

Hodgkin, S. T., Irwin, M. J., Hewett, P. C., & Warren, S. J. 2009, *MNRAS*, 394, 675

Huang, K. Y., Urata, Y., Kuo, P. H., et al. 2007, *ApJL*, 654, L25

Kennicutt, R. C., Jr. 1998, *ARA&A*, 36, 189

King, O. G., Blinov, D., Giannios, D., et al. 2014, *MNRAS*, 445, L114

Klein, C. R., Kubánek, P., Butler, N. R., et al. 2012, *Proc. SPIE*, 8453, 84532S

Krühler, T., Fynbo, J. P. U., Geier, S., et al. 2012, *A&A*, 546, A8

Lang, D., Hogg, D. W., Mierle, K., Blanton, M., & Roweis, S. 2010, *AJ*, 139, 1782

Lee, I., Im, M., & Urata, Y. 2010, *Journal of Korean Astronomical Society*, 43, 95

McMullin, J. P., Waters, B., Schiebel, D., Young, W., & Golap, K. 2007, *Astronomical Data Analysis Software and Systems XVI*, 376, 127

Michałowski, M. J., Kamble, A., Hjorth, J., et al. 2012, *ApJ*, 755, 85

Miyazaki, S., et al. 2002, *PASJ*, 54, 833

Ono, Y., Ouchi, M., Kurono, Y., & Momose, R. 2014, *ApJ*, 795, 5

Ouchi, M., Shimasaku, K., Okamura, S., et al. 2004, *ApJ*, 611, 660

Sari, R., Piran, T., & Halpern, J. P. 1999, *ApJL*, 519, L17

Schlaflly, E. F., & Finkbeiner, D. P. 2011, *ApJ*, 737, 103

Sheth, K., Frail, D. A., White, S., et al. 2003, *ApJL*, 595, L33

Troja, E., Barthelmy, S. D., Baumgartner, W. H., et al. 2013, *GRB Coordinates Network*, 15402, 1

Troja, E., Cusumano, G., O'Brien, P. T., et al. 2007, *ApJ*, 665, 599

de Ugarte Postigo, A., Lundgren, A., Martín, S., et al. 2012, *A&A*, 538, A44

Uhm, Z. L., & Zhang, B. 2014, *ApJ*, 780, 82

Urata, Y., et al. 2007, *ApJL*, 668, L95

Urata, Y., Huang, K., Takahashi, S., et al. 2014, *ApJ*, 789, 146

Urata, Y., Huang, K., Asada, K., et al. 2015, *Advances in Astronomy*, 2015, 165030

Urata, Y., Huang, K., Yamazaki, R., & Sakamoto, T. 2015, *ApJ*, 806, 222

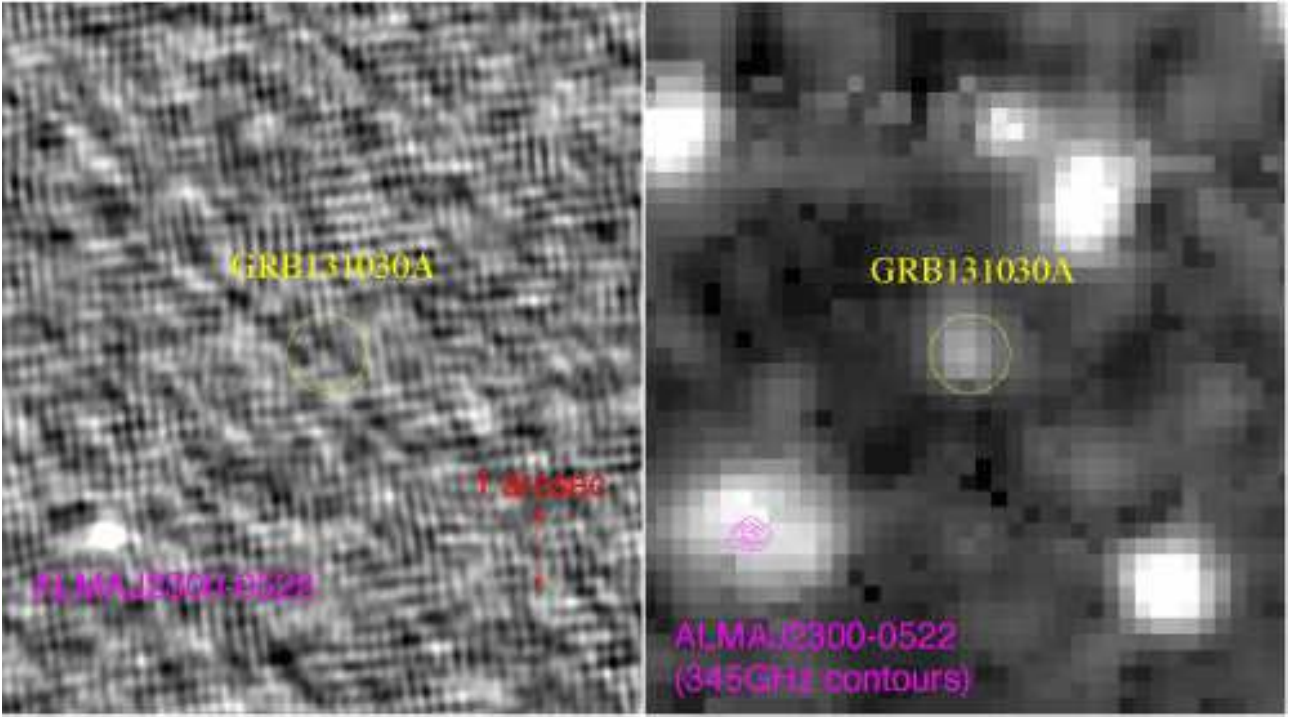


Fig. 1. Images of the GRB 131030A field in the 345-GHz band that were obtained using ALMA (left) and in the optical *Rc*-band that were obtained using SUBARU (right). The host galaxy of GRB 131030A was detected in the *Rc*-band image. The submm source is located $3''.5$ away from the GRB position with an optical counterpart. The magenta lines in the right panel display the contour (start from 2.5σ with 2.5σ step) of the ALMA image.

Wang, W.-H., Chen, H.-W., & Huang, K.-Y. 2012, *ApJL*, 761, L32

Watson, A. M., Richer, M. G., Bloom, J. S., et al. 2012, *Proc. SPIE*, 8444, 84445L

Xu, D., Fynbo, J. P. U., Jakobsson, P., et al. 2013, *GRB Coordinates Network*, 15407, 1

Zhang, B., & Mészáros, P. 2001, *ApJL*, 552, L35

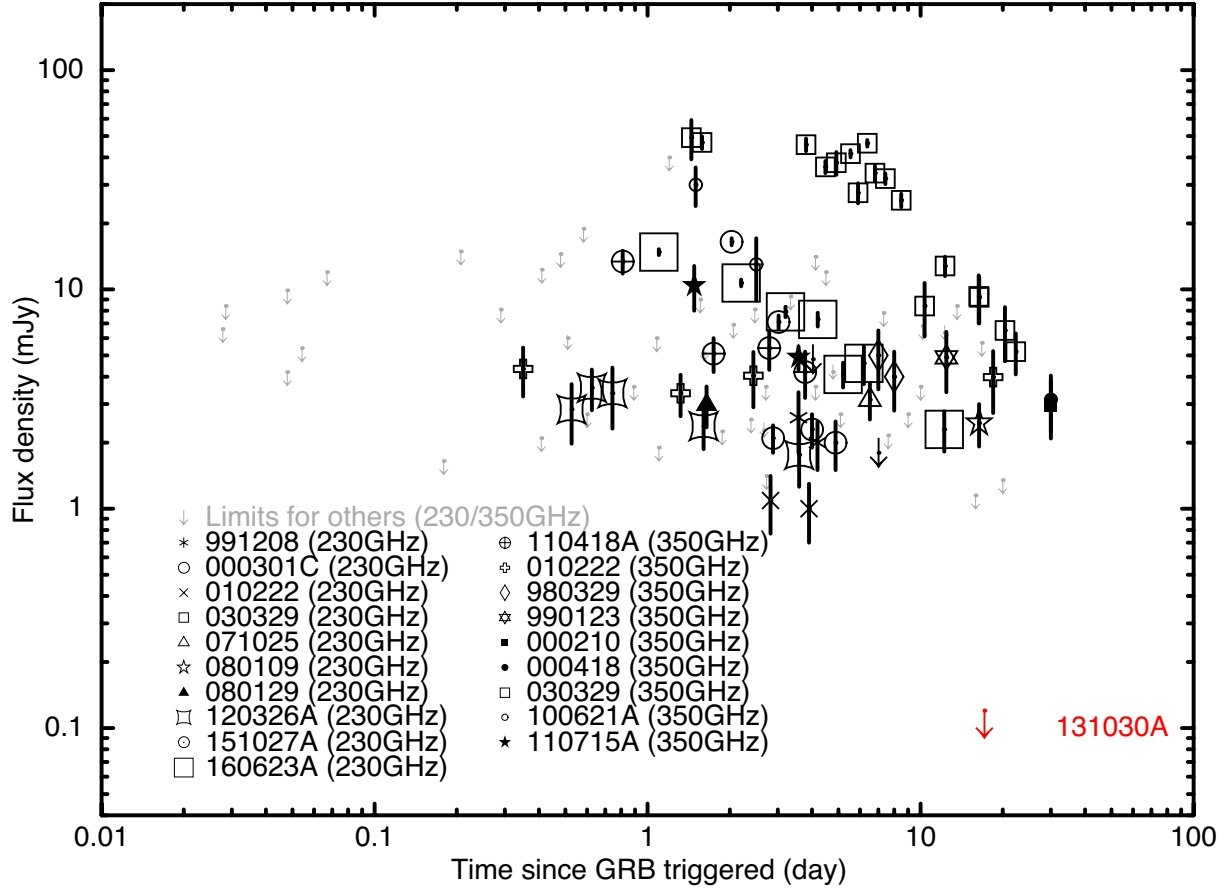


Fig. 2. Light curve summary of afterglow observations in submm bands (230 and 345 GHz). The ALMA observation for GRB131030A is significantly deep among other observations.

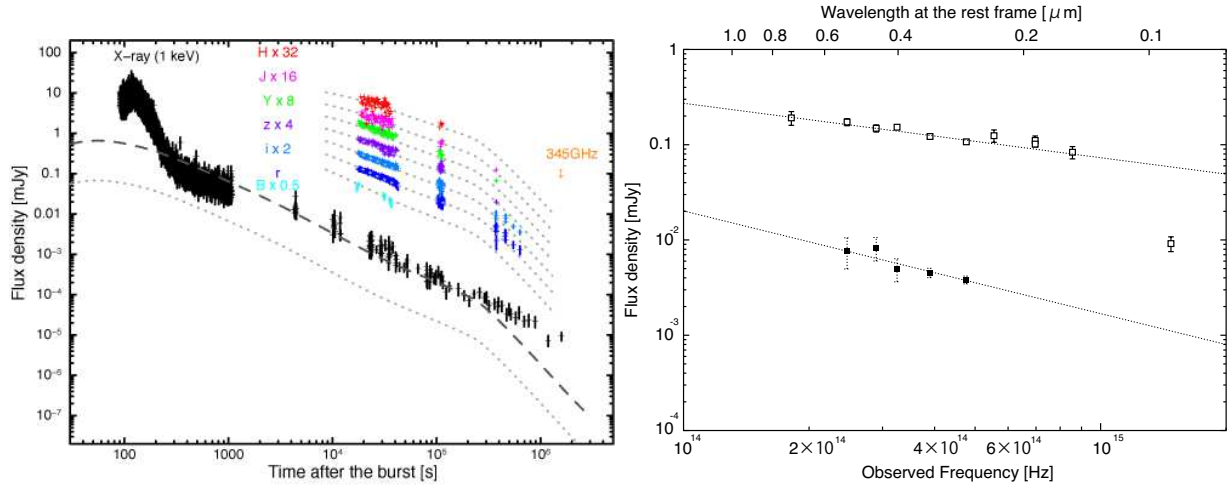


Fig. 3. Left panel shows X-ray, optical and submillimeter light curves of the GRB 131030A afterglow. The light-gray dotted lines indicate the optimal modeling functions obtained through the numerical simulation by the boxfit code. The dark-gray dashed line indicates the model function including the SSC component. The right panel shows the SED of the afterglow at 2.32×10^4 s (0.268 d; open squares) and 3.76×10^5 s (4.34 d; filled squares).

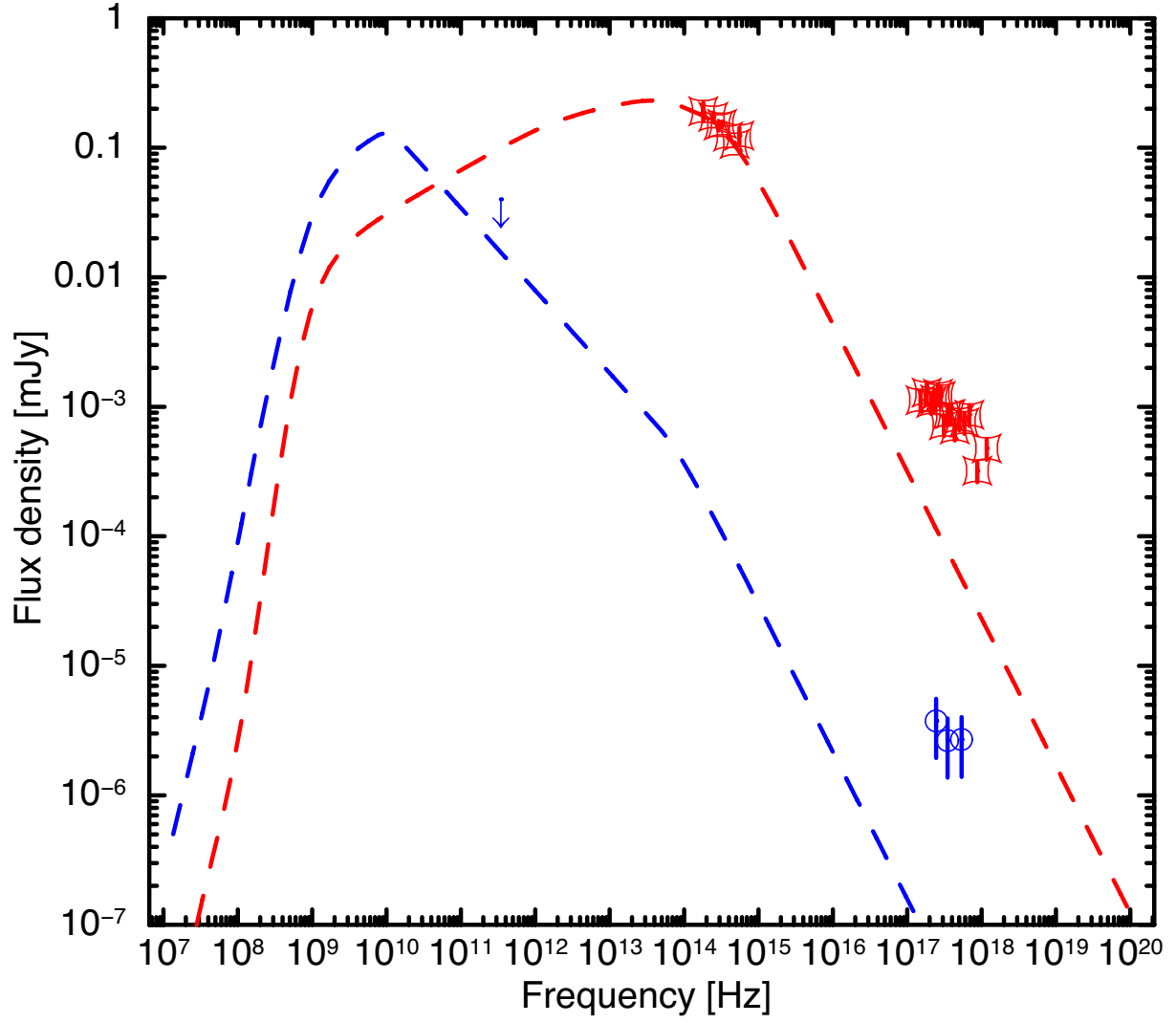


Fig. 4. Spectrum energy distribution at 0.2662 d (red) and 17.125 d (blue) after the burst. The dashed lines represent the forward shock synchrotron model spectrum that was calculated using the boxfit code. The ALMA 1- σ upper limit at 17.125 d is indicated by the blue arrow.

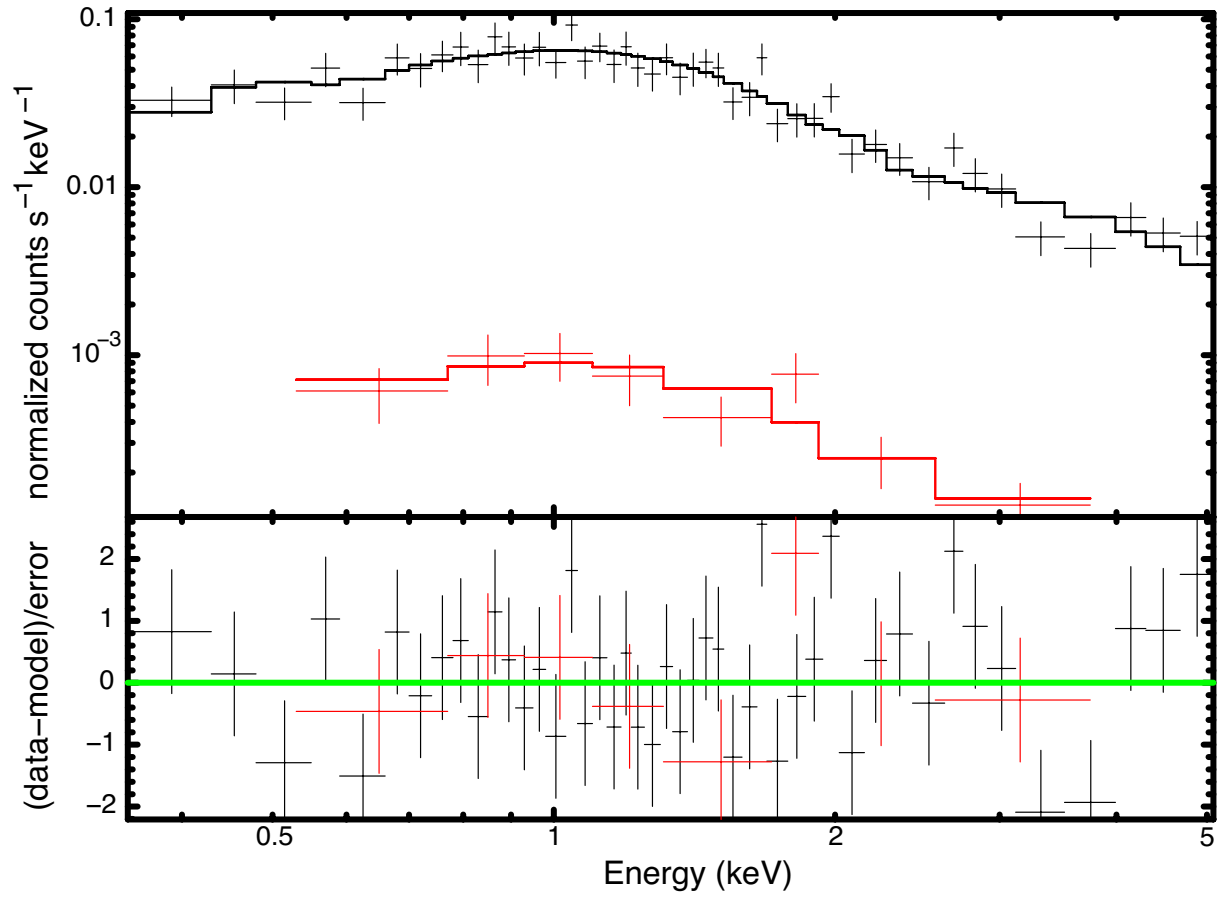


Fig. 5. X-ray spectrum in the time range of $1 \times 10^4 - 1 \times 10^5 \text{ s}$ (black cross) and $> 5 \times 10^5 \text{ s}$ (red cross). The bottom panel shows residual for fitting with power law.

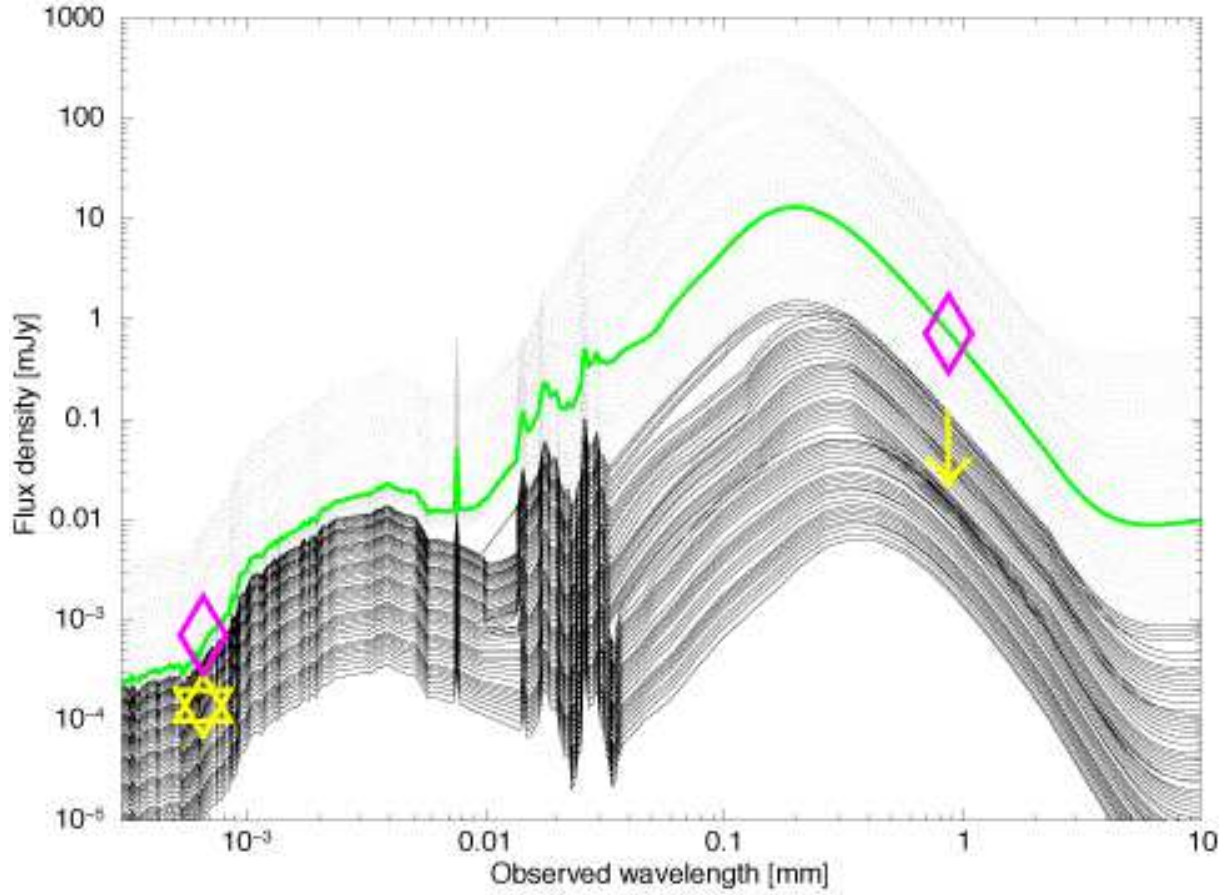


Fig. 6. SED of the GRB host galaxy and ALMAJ2300-0522. ALMA and SUBARU observations are indicated with yellow marks for the GRB host galaxy and purple diamonds for ALMAJ2300-0522. The ALMA observation constrains the infrared SEDs of the GRB host galaxy with the SED templates. The black thick curves represent the templates that satisfy the ALMA $3\text{-}\sigma$ upper limit for the GRB host galaxy. The green solid line indicates the optimal template for ALMAJ2300-0522, on the basis of assuming the same redshift as that of GRB131030A.

Table 1. Summary

| | | of | lightcurve | |
|---------------------------------|---|-------------------|--------------------------------------|-------------------|
| Single PL | | | | |
| | Earlier phase | | Later phase | |
| | $(1 \times 10^4 < t < 2 \times 10^5 \text{ s})$ | | $(t > \sim 2 \times 10^5 \text{ s})$ | |
| Filter | α | $\chi^2/\nu(\nu)$ | α | $\chi^2/\nu(\nu)$ |
| <i>B</i> | -1.17 ± 0.15 | 2.8 (4) | ... | ... |
| <i>r</i> | -1.00 ± 0.01 | 1.58 (307) | -2.08 ± 0.33 | 1.04 (11) |
| <i>i</i> | -0.99 ± 0.01 | 1.37 (300) | -2.07 ± 0.36 | 0.83 (6) |
| <i>z</i> | -0.97 ± 0.02 | 1.87 (130) | ... | ... |
| <i>Y</i> | -0.95 ± 0.02 | 1.25 (106) | ... | ... |
| <i>J</i> | -0.96 ± 0.04 | 1.79 (92) | ... | ... |
| <i>H</i> | -0.94 ± 0.07 | 2.02 (79) | ... | ... |
| X-ray | -1.31 ± 0.04 | 0.97 (94) | -1.29 ± 0.10 | 0.78 (18) |
| $(t > 4 \times 10^3 \text{ s})$ | | | | |
| X-ray | -1.25 ± 0.02 | 0.91 (125) | ... | ... |
| Broken PL | | | | |
| Filter | α_1 | α_2 | $t_b(\text{s})$ | χ^2/ν |
| <i>r</i> | -0.86 ± 0.04 | -2.06 ± 0.16 | $(2.51 \pm 0.48) \times 10^5$ | 1.41 (316) |
| <i>i</i> | -0.82 ± 0.04 | -2.04 ± 0.17 | $(2.51 \pm 0.48) \times 10^5$ | 1.22 (304) |

fitting.